Monte Carlo Simulation of Interlamellar Isotactic Polypropylene

Vikram K. Kuppa, Pieter J. in 't Veld,† and Gregory C. Rutledge*

Department of Chemical Engineering, Massachusetts Institute of Technology, Cambridge, Massachusetts 02139

Received February 14, 2007; Revised Manuscript Received April 9, 2007

ABSTRACT: Monte Carlo molecular simulations are reported to investigate the amorphous region between crystalline lamellae of isotactic polypropylene (*i*PP). It is the first such study in which consideration is given to the nature of pendant side groups on the polymer chain. The crystalline lamellae are modeled after the α_2 crystal of *i*PP, while the interphase and amorphous domains are equilibrated with respect to both spatial and topological degrees of freedom. A united atom force field is used to describe the interactions between the methyl, methylene, and methyne moieties that constitute a polypropylene molecule. Mass density and bond orientational order profiles, distributions of chain populations, interphase thicknesses, interfacial energies, local conformations as characterized by torsional angle sequences, and chain reentry statistics are studied for three different temperatures. Our results match well with the available experimental data and provide a molecular level understanding of the semicrystalline interphase for isotactic polypropylene. A comparison with linear polyethylene (PE) reveals the effects of chemical architecture on the crystal−amorphous interphase in semicrystalline polymers.

1. Introduction

Semicrystalline polymers have found widespread use due to their excellent mechanical and barrier properties. The crystallization of polymers corresponds to a first-order phase transition,[1] similar to other substances. However, a significant difference between long chain molecules and their low molecular weight counterparts lies in the kinetics of the crystallization process, because of which the complete incorporation of polymer molecules into the ordered crystalline state is rarely achieved. Thus, "semicrystalline" polymers are structurally nonhomogeneous materials and invariably consist of an intimate mixture of crystalline and amorphous phases. These polymers exhibit properties that are a consequence of the combined attributes of ordered (crystalline) and disordered (amorphous) constituent regions, with the unique feature that both crystalline and noncrystalline elements are topologically connected by chains that meander their way from region to region. A comprehensive understanding of the behavior of semicrystalline polymers thus demands extensive knowledge not only of the individual phases but also the interplay between them.

The existence and lamellar nature of semicrystalline polymers have been known for approximately half a century.[2−8] Various facets that describe the state of the semicrystalline system can be identified, including the gross morphological structure, degree of crystallinity, crystal unit cell structure, distribution of crystallite thicknesses and interlamellar spacings, and the widths of the amorphous regions and the interphase. It is difficult to probe experimentally the direct responses of the purely crystalline and amorphous regions due to the close proximity and interpenetration of the different phases. In addition, the transition from perfect crystalline order to the isotropy of the adjoining amorphous state in a lamellar semicrystalline polymer is accomplished over a third region of finite thickness, described by Flory and called the "interphase".[9] Calorimetric techniques like differential scanning calorimetry (DSC) that investigate the thermal properties of a material,[10] scattering techniques like small-angle neutron scattering, X-ray diffraction, and light scattering,[11−13] and more local probes such as NMR, Raman, and IR spectroscopy[14,15] have been used to estimate the fractions of crystalline, amorphous, and interphase material. For the case of isotactic polypropylene (*i*PP), high-resolution solid-state NMR[16] has been particularly useful to study the phase structure of *i*PP isothermally crystallized from the melt. Analysis of the ^{13}C spin−lattice relaxation spectra indicated three populations, identified with distinct crystalline, amorphous, and a rigid yet noncrystalline region, presumed to be the interphase. The amount of total interphase material was found to decrease from approximately 27% at 296 K down to about 8% at 408 K. Analysis of Raman spectra for semicrystalline *i*PP by Nielsen and co-workers[17] also indicated three separate regions, corresponding to Raman bands associated with different conformational states. In a third study, Bond et al.[18] used wide- and small-angle X-ray scattering (WAXS, SAXS) and DSC to determine the long periods, crystalline fractions, and "fold surface" free energies for several different polypropylenes synthesized using Ziegler−Natta and metallocene catalysts.

In this paper, we use Monte Carlo molecular simulations to study semicrystalline isotactic polypropylene, focusing on a detailed molecular level description of the intercrystalline region between lamellae comprised of the α_2 crystal structure of *i*PP. Crystal and amorphous regions coexist in a metastable equilibrium that is maintained by imposing the following constraints: (1) maintaining a constant density in the interlamellar region that is lower than the perfect crystal density and (2) holding the polymer crystal structure fixed throughout the simulations. This study is the first step in moving beyond the prototypical linear polymer, polyethylene (PE), to consider the influence of simple side groups. Our ultimate goal is to reveal the influence of chemical architecture on the correlation between morphology and the properties exhibited by semicrystalline polymers. We begin by describing in section 2 the force field interactions, Monte Carlo methods, and the setup of the simulation. In section 3 we discuss our results and compare and contrast *i*PP and PE, before finally concluding in section 4 with a broad overview of our study.

* Corresponding author: e-mail rutledge@mit.edu.
† Current address: Sandia National Laboratories, MS 1415, Albuquerque, NM 87185.

10.1021/ma0703958 CCC: $37.00
Published on Web 06/07/2007

2. Methods

2.1. Force Field. We used the force field developed by Pütz et al.[19] to simulate semicrystalline *i*PP. This model was based on the TRAPP force field developed by Martin and Siepmann[20] and was optimized to give correct results for the coexistence curve of 2-methylpropane near the vapor−liquid critical point. In addition, the force field was validated by comparing structure factors calculated from simulations with X-ray scattering data, and by matching cohesive energy densities with experimental results, for high molecular weight isotactic polypropylene. The force field represents the methyne (−CH−), methylene ($-CH_2-$), and the methyl ($-CH_3$) groups of polypropylene as united atoms or "beads". Nonbonded interactions between beads separated by four or more bonds along the *i*PP chain are approximated by the standard Lennard-Jones (LJ) function:

$$E_{ij}^{\mathrm{LJ}} = 4\epsilon_{ij}\{(\sigma_{ij}/r_{ij})^{12} - (\sigma_{ij}/r_{ij})^{6}\} \tag{1}$$

where $r_{ij} = |\mathbf{r}_i - \mathbf{r}_j|$ is the distance between beads i and j. The LJ interactions are truncated at a distance of $2.5\sigma_{ij}$, and long-range corrections to the potential are applied as mentioned in ref 21. Values of ϵ and σ for (−CH−), ($-CH_2-$), and ($-CH_3$) are {0.0828, 0.3818, 0.8139} kJ/mol and {0.468, 0.395, 0.373} nm, respectively. Interactions between unlike beads are calculated using the Lorentz−Berthelot rules.[22]

Bonded interactions that act upon two or more adjacent beads along the chain are composed of four different energetic potentials. Bond stretching is represented by a simple springlike stretching potential:

$$E_{ij}^{\mathrm{bond}} = \frac{1}{2}k_{ij}^{\mathrm{B}}(r_{ij} - l_0)^2 \tag{2}$$

with $k_{ij}^{\mathrm{B}} = 3.761$ MJ/(mol nm^2) and the equilibrium bond length $l_0 = 0.154$ nm for all pairs of beads (i and j) directly bonded to each other. The bond angle bending potential is modeled using

$$E_{ijk}^{\mathrm{angle}} = \frac{1}{2}k_{ijk}^{\mathrm{A}}(\theta_{ijk} - \theta_0)^2 \tag{3}$$

where θ_{ijk} is the angle defined by two consecutive bonds at atom j, $k_{ijk}^{\mathrm{A}} = 518.12$ kJ/mol, and $\theta_0 = 112°$ and 114° when the central bead in the angle is −CH− and $-CH_2-$, respectively. Dihedral angle potentials to simulate chain stiffness are incorporated via the use of a rotational potential defined by four nearest neighbors along the chain:

$$E_{ijkl}^{\mathrm{dihedral}} = \sum_{p=0}^{3} k_{\mathrm{p}}^{\mathrm{D}} \cos^p \phi_{ijkl} \tag{4}$$

where ϕ_{ijkl} is the dihedral angle constructed by three consecutive bonds. The torsional prefactors are $k_{\mathrm{p}}^{\mathrm{D}} \equiv \{3.282, 7.432, 1.857, -14.657\}$ kJ/mol.

In isotactic polypropylene, all of the $-CH_3$ side groups on a single chain are constrained to be on one side of the all-trans backbone. In explicit atom models, the chiralty of each methyne site is ensured by the hydrogen atom, which prevents "flipping" of the methyl group. In the united atom model employed here, chirality (and thus tacticity) is maintained by the use of an improper dihedral potential that forces the methyl side groups to stay always on the same side of the chain with respect to each other. This potential is modeled as follows:

$$E_{ijkl}^{\mathrm{improper}} = \frac{1}{2}k_{ijkl}^{\mathrm{I}}(\psi_{ijkl} - \psi_0)^2 \tag{5}$$

where ψ is the angle between two planes defined by (CH_2, CH_3, CH_2) and (CH_2, CH, CH_2) triplets sharing common methylene groups. $k_{ijkl}^{\mathrm{I}} = 518.12$ kJ/mol, equal to that of the angle bending potentials, while $\psi_0 = \pm 30.25°$ depending on chain tacticity.

2.2. Simulation Setup and Details. 2.2.1. Monte Carlo Moves. Our simulations of the interphase were conducted in the (N, n, V, T, μ) ensemble, where the chemical potential associated with each individual bead is assumed to be constant, and the chemical potential μ_k for a chain of k beads is $\mu_k = ((k - i)/(j - i))\mu_j - ((k - j)/(i - j))\mu_i$; μ_i and μ_j are two potentials whose values are fixed implicitly by the constraints on the number of beads N and the number of chains n. We employ a suite of Monte Carlo moves that includes site displacement, reptation, rebridging (RB), end-bridging (EB), extended configurational bias (ECB), and expanded ensemble replica exchange. The first four moves have also been used earlier to study the interlamellar phase for linear PE chains and have been suitably modified in the current investigation to account for the methyl side groups of *i*PP. The rebridging[23] and end-bridging algorithms,[24] which were initially developed for linear chains, are performed by excising a trimer of beads from a chosen chain and inserting them back on the same chain (rebridging) or attached to the free end of another randomly selected chain (end-bridging). During the bridging process, closure is accomplished by solving the geometric system of equations that give feasible solutions for the rebridging of a trimer in space, while keeping the bond lengths and angles associated with each excised bead unchanged. Extension of the EB and RB moves to branched polymers is achieved by fixing the side-group conformation (trivial in the case of methyl groups) and applying to it the same torsional flip as is given to the main chain bead to which it is connected, so as to maintain the relative positions of these beads with respect to the main chain and to each other. Initial and final positions of all the beads displaced during the cutting and bridging process are used to calculate the energy change accompanying the move. To preserve detailed balance, Jacobians corresponding to the transformation of coordinates from Cartesian to spherical are incorporated into the acceptance criterion, as explained previously.[23]

The primary difference between the molecular architectures of *i*PP and linear alkanes like PE is the methyl side group on every second bead of the polypropylene backbone. To simulate this new chain architecture efficiently, two new moves are introduced in addition to those which have previously been used to simulate freely rotating chains (FRC) and PE,[21,25,26] described above. One is the expanded ensemble technique (discussed in the next section), and the other is an extension of the simple reptation algorithm fashioned after the extended configurational bias method of Karaiskos et al.[27] For linear polymers, reptation is accomplished by excising and regrowing single beads from the ends of chains. In our implementation, a randomly chosen number of propylene monomers are removed from the end of a chain that is terminated by a free (untethered) bead. A biasing potential that depends on the nonbonded (LJ) energies[28] is introduced in an attempt to add the expunged segments to the free end of any chain (same or different) chosen at random. The bias is then removed in the final acceptance step.

All the MC moves, including those that exchange beads between chains, like the end-bridging,[23,24] reptation, and the extended configuration bias,[27] were modified to reject any trial that altered the regular head-to-tail structure of the *i*PP chains. The minimum permitted length of a tail was 3 beads, the

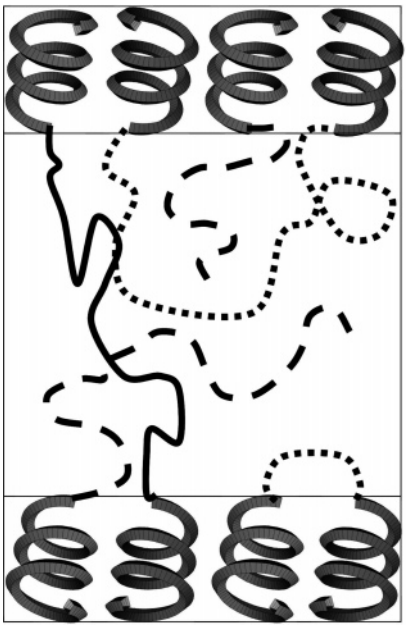

Figure 1. Schematic of the simulation box showing helical chains at the top and bottom, in crystallographic registry. Mobile chains in the interphase are represented by bridges (solid curve), loops (dashed curve), and tails (long-dashed curve).

minimum permitted length of a loop was 8 beads, and the maximum permitted length of any chain was 1000 beads. Any move that resulted in a situation where these rules were violated was automatically rejected. Upon application of this MC move suite, the noncrystalline interlamellar region of the simulation equilibrates fully with respect to both spatial and topological degrees of freedom, subject only to the constraints imposed by the crystalline boundaries at $Z = 0$ and $Z = L$ and the imposed density of the interlamellar region. The resulting ensemble consists entirely of tails, loops, and bridges, as shown in a schematic of the simulation box in Figure 1. The fraction of tails is determined by the fraction of end beads included in the simulation; the remainder is divided among loops and bridges according to the equilibrium statistics. It is important to note that all chains are tethered at one or both ends to a crystal stem at $Z = 0$ or $Z = L$, but the regularity (or lack thereof) of the topology between tether points is determined solely by equilibration of the ensemble, as is the length distribution of each population (tails, loops, bridges). The end-bridging move is especially important since it alters the molecular features of pairs of chains, resulting in chains of different conjunction with respect to the crystal surfaces and permitting the simulation to sample an ensemble in which the structures of chain molecules differ in both spatial arrangement of beads and the topological connectivity between the amorphous and crystalline regions.

2.2.2. The Expanded Ensemble Method. Studies of interphase models for FRC and PE have demonstrated the effectiveness of parallel tempering in temperature space.[21,25,29] In those investigations, a swapping criterion for multicanonical algorithms derived by Kofke[30] was used to perform simultaneous runs on several different processors, each processor running the simulation at a different temperature. Using this method, systems at temperatures well below and well above the melting point of PE were simulated simultaneously. The exchange of configurations between different thermodynamic states was performed according to a simple Metropolis criterion.[21] Apart from the ease of sampling, the parallel tempering method also allowed the simultaneous determination of system properties at different temperatures in a single run.

This same technique of parallel tempering between states at different temperatures was initially attempted for *i*PP, but without any marked success. Even for temperatures well above the melting point of *i*PP ($T_m \approx 450$ K), the system was essentially "frozen" in space; the acceptance of chain length altering MC moves such as EB and ECB was extremely low. The distinction in behavior between PE and *i*PP semicrystalline systems can be traced to the difference in chain architecture arising from the presence of the methyl side group on *i*PP. Most new conformations generated by performing MC moves result in configurations with large degrees of overlap between the methyl side groups and other groups, with huge energy penalties. Thus, the protruding methyl beads are the crucial difference between PE and PP and prevent the facile acceptance of attempted moves. This scenario is especially true for some of the more "advanced" Monte Carlo moves developed for polymers like reptation, ECB, and EB, the acceptance ratios for which are orders of magnitude lower for *i*PP than for PE. In addition, because of the imposed constraints on chain length and structure as well as restrictions on tacticity, moves like EB have a smaller number of allowed sites on the molecular backbones to target.

To overcome the problem of low acceptance and to sample phase space in an effective manner, we developed a multicanonical replica exchange method in Hamiltonian space,[31,32] in which the methyl side group interactions are different on each processor (system state). The energy of interaction of the methyl side groups are modified so that in the Lennard-Jones potential function of eq 1 the energy parameter ϵ_{i,CH_3} is now a function of the particular system state p:

$$\epsilon^p_{CH_3} = f(p)\epsilon_{CH_3} \qquad (6)$$

$$\epsilon^p_{i,CH_3} = (\epsilon_i \epsilon^p_{CH_3})^{1/2}$$

$$f(p) = \{1, 0.92, 0.83, 0.76, 0.69, 0.63, 0.57, 0.53, 0.48, 0.43\}$$

$$p = 1, 2, 3, ..., 10$$

The relevant LJ potential now becomes

$$E^{LJ}_{i,CH_3}(\epsilon,\sigma,p,r) = 4\epsilon^p_{i,CH_3}\{(\sigma_{ij}/r_{ij})^{12} - (\sigma_{ij}/r_{ij})^6\} \qquad (7)$$

We simultaneously ran 10 systems at the same temperature on 10 different processors. Each system corresponds to a single state, whose Hamiltonian is modified by changing the interaction potential for the methyl side group, as shown in eqs 6 and 7. Periodically, swaps are attempted between adjacent states and accepted or rejected according to the following Metropolis criterion:

$$P^{1\rightarrow 2}_{acc} = \min[1, \exp(-\beta(H_2\{\mathbf{r}_1\} + H_1\{\mathbf{r}_2\} - H_2\{\mathbf{r}_2\} - H_1\{\mathbf{r}_1\}))] \qquad (8)$$

where $H = \sum_{i,j} E^{LJ}_{ij}$ and $\{\mathbf{r}_1\}$ and $\{\mathbf{r}_2\}$ are the coordinate sets of the systems being exchanged, while the subscripts 1 and 2 denote the two system states. The interaction potentials are modified (as described by eqs 6 and 7) by changing $f(p)$ values to maintain equal swapping probabilities (≈20%) between adjacent states, similar to the methodology used to optimize parallel tempering in temperature space.[30] A schematic for exchange of replicas between states is shown in Figure 2. The advantage of such Hamiltonian replica exchange moves is that states at the low end of the interaction spectrum are much more

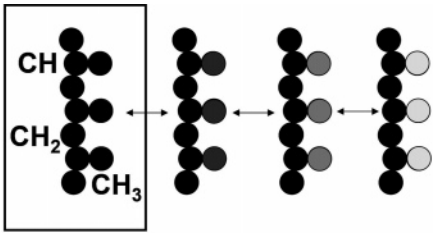

Figure 2. Schematic illustrating the expanded ensemble used to promote sampling of phase space. Fractions of an *i*PP chain in four different systems, with different side group methyl interactions are shown from left to right, in which the magnitudes of nonbonded interactions are shown in grayscale. The complete chain with full interactions (in black) is highlighted, at the extreme left.

easily sampled than those at the high end. We are interested ultimately only in the realistic system, with the complete interaction potential ($f(p) = 1$), which now explores phase space by virtue of configuration exchange with more rapidly equilibrated states. The benefit of using this scheme can be quantified by monitoring the end-to-end vectors of all chains and the position vectors of all mobile beads (with origin at the center of the simulation box). The autocorrelation functions decay with a half-life of about 5000 cycles for the end-to-end vectors and about 2×10^4 cycles for the bead position vectors. As expected for an anisotropic system with tethered chains, neither value decays completely to zero; the end-to-end vector autocorrelation decays to $\approx$0.05, while the bead position vector autocorrelation decays to $\approx$0.19. In addition, an estimate of the mean-square displacement of beads over the course of the simulation indicates that beads are able to sample adequately the simulation box. Without employing the expanded ensemble technique, effective simulation of these quasi-linear systems would have been impractical.

2.3. Initial Structure. The lowest energy ("crystalline") conformation of an individual *i*PP molecule is the 3/1 helix created by successive *trans* and *gauche* dihedrals along the chain. Because of the presence of the asymmetrically substituted methyl groups, both right- and left-handed helices (*d* and *l* stereoisomers) are possible and isoenergetic. Furthermore, the projection of the methyl groups imparts a direction to each helix. Thus, there are four distinct possible chains in the crystal: left-up, right-up, left-down, and right-down. Intermolecular energies vary with the packing geometry, resulting in four possible polymorphs for *i*PP: the crystal structures α, β, γ, and the quenched form. Of these four, the α[33,34] phase is the most commonplace and occurs in α_1 and α_2 variants. We used the α_2 form, which belongs to the $P2_1/c$ space group and consists of sheets of isoclined, isochiral helices to represent the crystalline lamellae that bound the noncrystalline interlamellar region. The unit cell is monoclinic and consists of four chain segments of three repeat units, one each of left-up, right-up, left-down, and right-down helices, for a total of 12 repeating units. Its dimensions are $a = 0.666$ nm, $b = 2.08$ nm, $c = 0.65$ nm, $\alpha = \gamma = 90°$, and $\beta = 99.6°$. The crystallographic density is 0.95 g/cm^3.

The simulation box for *i*PP was constructed in a manner similar to that followed for polyethylene.[25,29] Initially, 40 chains with 127 beads each were assembled in 3/1 helical crystal conformations with handedness and direction for each chain commensurate with the α_2 structure. The simulation box thus constructed was made up of 140 repetitions of the primitive unit cell (5, 2, and 14 in the *X*, *Y*, and *Z* directions, respectively). The most common lamellar surface observed for *i*PP in the monoclinic α_2 phase is {001},[35] which means that the axes of chains through it are inclined at an angle of 9.6° with respect to the lamellar normal (*Z* axis). After construction of the crystalline block, beads were deleted at random from the center of the simulation box to achieve a density of 0.77 g/cm^3; upon subsequent equilibration of the density profile across the interphase, the desired, experimentally determined melt density[36] of 0.75 g/cm^3 is obtained near the center plane of the simulation box. Crystal stems were simulated by keeping 19 beads in the tethered part of each chain fixed in their helical conformations. Melting of the crystalline lamellae is precluded by immobilization of these crystal sites. Thus, after the desired average density is achieved by deletion of beads, the simulation box was comprised of $n = 2824$ sites distributed among 40 "tails" or chain ends and 20 "bridges" or tie molecules. All tails were terminated by $-CH_2(CH_3)$ groups, while loops and bridges were tethered at both ends to $-CH_2-$ groups belonging to the lamellae; these beads constitute the last of the fixed beads in the crystal block and hence form the crystal surface. The interlamellar spacing between the crystalline lamellae was 6.5 nm, which matches perfectly with experimental values obtained from the long period and crystalline fraction of *i*PP, as obtained from XRD studies.[18] Assuming a lamellar thickness corresponding to $\sim$150 beads and the statistical analysis described previously,[37] the molecular weight for *i*PP simulated here was estimated to be to be $\sim$8750 kg/mol. The final dimensions of the simulation box were (3.33, 4.16, 9.1) nm in the *X*, *Y*, and *Z* dimensions, respectively. The system was initially subjected to 10^4 cycles each at 10 000, 5000, 1000, and 700 K, in a stepwise cooling regimen designed to randomize completely the structure of the noncrystalline interlamellar region. The system was then quenched to the desired temperature and allowed to equilibrate for 5×10^4 cycles. Production runs were 5×10^5 cycles long, and configurations were sampled every 5000 cycles. Error bars were calculated by independent sampling after every 1×10^5 cycles. Each cycle consists of *N* selections of MC moves, chosen with the following probabilities: end-rotation, 14%; site displacement, 50%; reptation, 7%; rebridging, 14%; end-bridging, 14%; ECB, 0.9%; and replica exchange, 0.1%. The right combination of moves is crucial, since one of the difficulties observed in a sluggish system such as this, especially for the end-bridging algorithm, is "shuttling"; i.e., accepted moves switch back and forth between the same initial and final states. This can be avoided by a judicious, random selection of attempted move types, such that between each accepted move of every type several other moves of a different kind are likely to be accepted. In addition to enhanced sampling, such a random application of selected Monte Carlo moves also maintains detailed balance.

3. Results and Discussion

Figure 3 shows the mass density profile of the system along the *Z* axis. Densities were computed for bins of size 0.027 nm, with the masses of all beads apportioned among bins according to the volume of each bead present in that particular bin. Since the top and bottom crystal surfaces are equivalent, the density profile is shown only for one-half of the simulation box, after averaging over both surfaces to improve statistics. The density shows a continuous and distinct shift from that of the pure crystal to that of an amorphous meltlike state, with an intervening transition zone or interphase. Using the concept of the Gibbs dividing surface (GDS),[29] the interface is introduced as an abrupt transition between the melt and crystal states. A simple mass

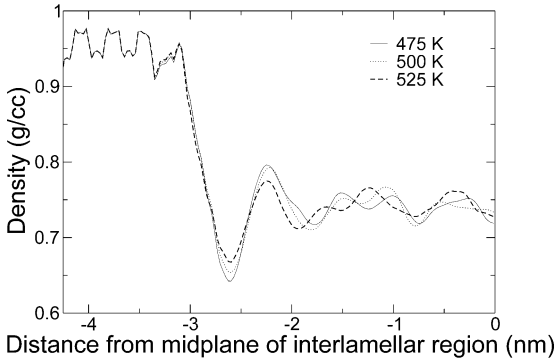

Figure 3. Mass density profiles for half of the simulation box from crystal (left) to melt (right) for 475, 500, and 525 K.

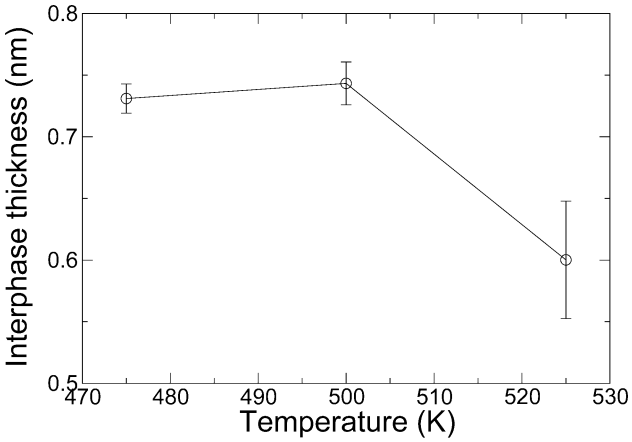

Figure 4. Interface thicknesses calculated from a Gibbs dividing surface analysis of mass densities as a function of temperature.

balance carried out across the density profile according to eq 9 delineates the position of the interface, Z_{int}:

$$\int_{-\infty}^{\infty} \rho^{\text{profile}}(z)\,dz = \int_{-\infty}^{z_{int}} \rho^{\text{crystal}}\,dz + \int_{z_{int}}^{\infty} \rho^{\text{melt}}\,dz \qquad (9)$$

The true metastasis between crystal and amorphous regions occurs over a finite interphase width which we define as twice the distance between the true crystal surface and the GDS. The interphase thickness is shown for three different temperatures in Figure 4. As shown previously for PE,[29] the thickness of the interphase decreases with temperature, since entropy favors an increase in the amorphous material at the expense of the interphase.

Figure 5 reveals the orientation profiles of the chains with respect to the *Z* axis of the simulation box; the inset shows with arrows the precise set of bonds used to calculate the orientational order parameter, P_2. The orientational order mimics the density profile, displaying the three different regions corresponding (from left to right in the figure) to the crystal, interphase, and unoriented amorphous material.

Figures 6, 7, and 8 show the population distributions of tails, loops, and bridges, respectively, normalized by the total number of chains in the system. The populations of chains follow an exponential decay as functions of the number of constituent beads. This result is a consequence of defining the chemical potential as described earlier and confirms the equilibration of chains within each population. Furthermore, for chains of length greater than 200 beads, the populations of loops and bridges are comparable, confirming equilibration between these two populations. The number of chains of a particular length is dictated by three different factors: local density, configurational

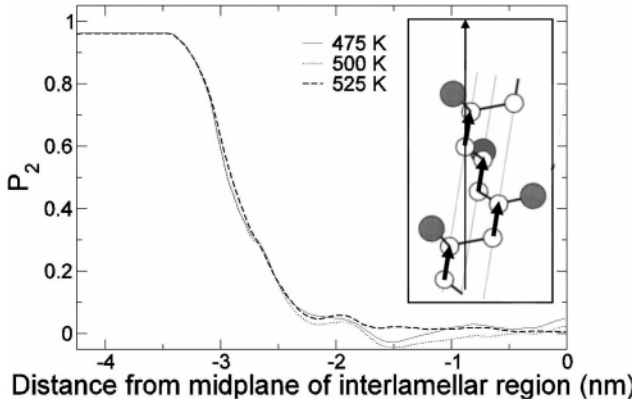

Figure 5. Orientation profiles calculated using the bond orientation parameter $P_2 = (3\cos^2(\theta) - 1)/2$ for 475, 500, and 525 K. Inset shows segment of *i*PP chain in helical conformation, with bold arrows indicating the bonds along the chain backbone used for calculation of P_2.

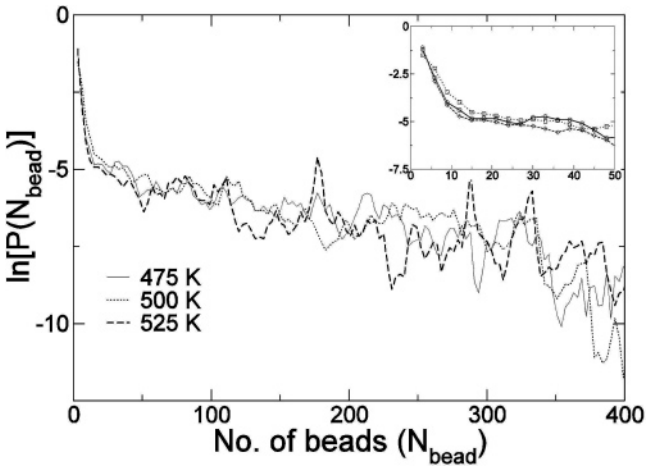

Figure 6. Population distributions of tails at 475, 500, and 525 K. Inset shows the behavior of short tails ($N_{bead} < 50$): 475 K (circles), 500 K (squares), and 525 K (diamonds).

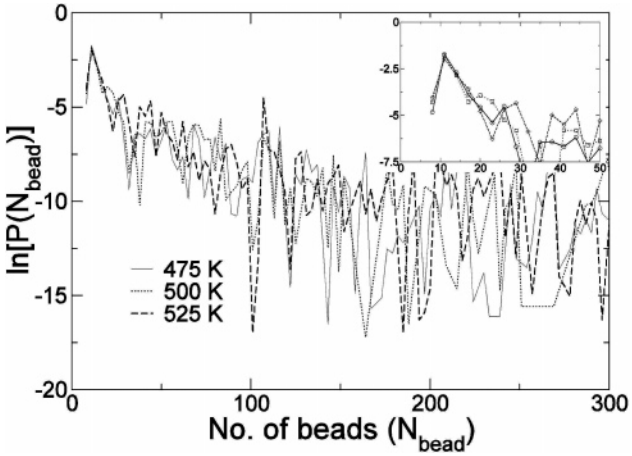

Figure 7. Population distributions of loops at 475, 500, and 525 K. Inset shows the behavior of short loops ($N_{bead} < 50$): 475 K (circles), 500 K (squares), and 525 K (diamonds).

energy of the chain segment, and temperature. It is possible for us to derive a chemical potential associated with each bead in a particular population. The Boltzmann probability for the existence of a chain segment of length N_{bead} is

$$\ln(P_{N_{bead}}) = -\beta[F + TS] + \beta\mu_{bead}N_{bead} \qquad (10)$$

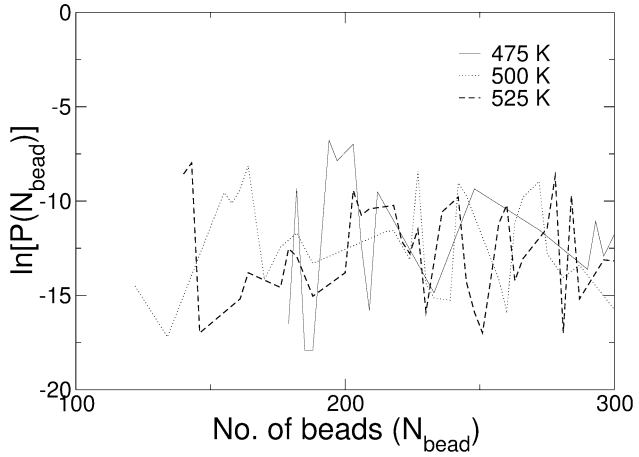

Figure 8. Population distributions of bridges at 475, 500, and 525 K.

Thus, from the slope of the lines in Figures 6 and 7, we can determine the excess chemical potential for a single bead. The value for $\mu_{bead} \approx -0.03$ kJ/mol, obtained from the slope of Figure 6 for tails; similar values are obtained from loops and bridges at large N_{bead}. By comparison, the chemical potential per bead from simulations of linear alkanes at 1.02 atm, which is slightly higher than the pressure in this study, was estimated to be $\mu_{bead}^{simulation} \approx -0.033$ kJ/mol, while the experimental value is $\mu_{bead}^{experiment} \approx -0.039$ kJ/mol (using the Peng−Robinson equation of state to fit the experimental data).[38,39] This is an important result since it validates not only the force field but also the MC sampling scheme. The population distributions of loops and tails have similar slopes, leading to the conclusion that for large chains (i.e., for chains that lie predominantly outside the interphase; see below) the chains segments are locally indistinguishable; most chain segments act like unconstrained amorphous material.

While energy and temperature largely dictate the populations of chains in the amorphous region of the noncrystalline domain, short chains and those that lie predominantly within the interphase are also influenced by the crystal surface. As is evident from Figures 6 and 7, the populations of short tails and loops behave in a manner markedly different from each other as well as from longer chains within the same population. Figure 9 shows the root-mean-square end-to-end distance as well as its Z component for tails of different lengths, at 475 K. The horizontal line denotes the distance corresponding to the position of the boundary of the interphase from the crystal plane (i.e., $2Z_{int}$, from eq 9). Tails of length greater than 15 beads extend beyond the interphase, and as seen in Figure 6, for these chains a steady exponential decay profile is established. Figure 10 shows the average distance from the crystal surface of beads in a loop ($\langle Z_{bead} \rangle$) as a function of loop length at 475 K. Long loops ($N_{bead} > 60$) have a large number of their constituent beads outside the interphase. Loops shorter than 60 beads, on the other hand, lie almost exclusively within the interphase. As seen in Figure 3, these loops are packed to a higher density than in the fully amorphous region of the interlamellar domain. Since the magnitude of chemical potential increases with density, loops shorter than 60 beads experience a higher chemical potential, which is also evidenced by the steeper slope in the population distribution of loops (Figure 7) for $N_{bead} < 60$. The same effect is seen in the tail population distribution for $N_{bead} < 15$ (Figure 6).

In addition to the exponential decay in the population distribution for loops with $N_{bead} > 60$ and the steeper slope for loops with $N_{bead} < 60$ due to density, there exists a maximum

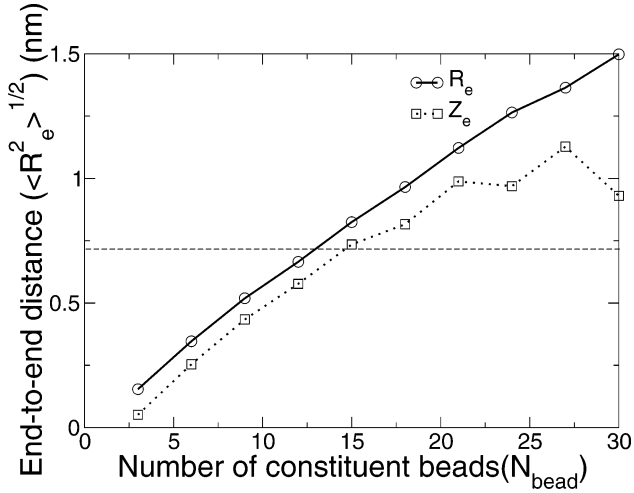

Figure 9. End-to-end distances (total, R_e, and Z direction, Z_e) of the mobile portion of tails as a function of tail length, at 475 K. Horizontal line shows interphase thickness. Chain lengths greater than about 15 beads extend beyond the interphase, away from the influence of the crystal.

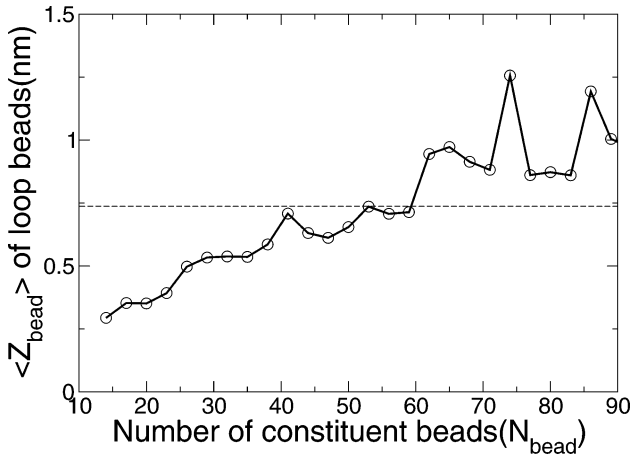

Figure 10. Average distance of loop segments from the crystal surface as a function of loop length, at 475 K. Horizontal line shows interphase thickness. Short loops lie entirely within the interphase.

in the loop distribution at $N_{bead} = 11$. No such maximum is observed for tails and bridges. To confirm that this result is not an artifact of the imposed minimum loop length at $N_{bead} = 8$, additional simulations were performed in which the minimum loop size was set to 11; in both cases, loops of 11 beads were most populous. The significantly antithetic behavior of the shortest loops, as compared to shortest tails, can be attributed to the influence of the crystal structure and to chain architecture. Since the loops are tethered at both ends, they are forced to adopt conformations that result in end-to-end vectors corresponding to specific reentry points dictated by the arrangement of atoms at the {001} surface of the α_2 unit cell. For linear FRCs, this restriction imposed on end-to-end spacing makes certain loops more propitious than others because the total number of allowed conformations that correspond to the specific end-to-end vector is higher for that particular chain length.[40] With the introduction of a dihedral potential (chain stiffness), the preference for selected loop lengths is accentuated. As discussed earlier, the lowest energy conformation of an *i*PP chain is the (crystalline) 3/1 helix consisting of alternating *trans* and *gauche* backbone dihedral sequences. In the amorphous region, entropy favors the introduction of less favorable conformations according to their Boltzmann probabilities. Since the loops connect two

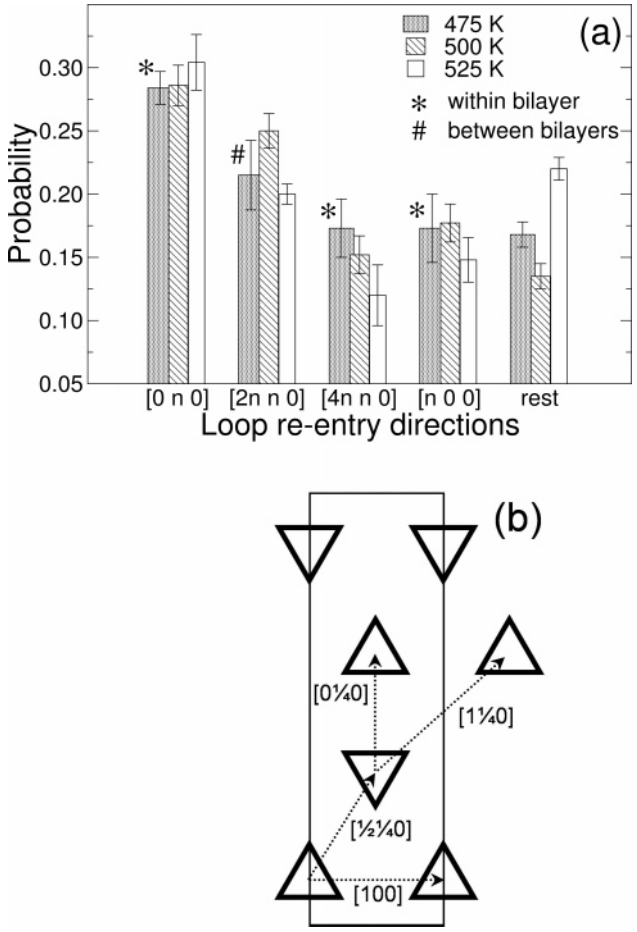

Figure 11. (a) Distribution of loop reentry direction vectors at 475, 500, and 525 K. (b) Schematic of unit cell, indicating prominent reentry direction vectors.

helical stems on the same lamella, their constitutive segments adopt dihedral sequences that adjoin the crystalline *trans*−*gauche* conformations. For short loops, i.e., "tight folds", the fraction of less favorable torsion sequences required to connect crystal stems is greater than that which would be predicted by the Boltzmann probability. Thus, the populations of the loop segments of length 8 is depressed relative to the population expected in a comparable amorphous phase. In this manner, we see that the structure of the underlying crystal surface precludes the occurrence of some short loops that would otherwise be more probable, based on configurational energy alone. This observation is substantiated by the variation of short loops with temperature. From 475 to 525 K, the number of loops that exist in the lowest allowed chain length (8) shows a 2-fold increase, from 0.8% to 1.7%, of the total number of chains in the system. With increasing temperature, the system tends to favor shorter loop lengths. This is in agreement with the increasing probability for the existence of higher energy dihedral sequences with increasing temperature.

It is instructive to examine the arrangement of loop tethering sites on the crystal surface. Following the terminology previously used for PE,[25] loop reentry statistics (end-to-end vectors of loop segments) are indicated by vectors [*m*, *n*, 0], where *m* and *n* are multiples of the projection of the *a* and *b* unit cell directions onto the *XY* plane. Figure 11 shows the crystallographic directions for loop reentry positions. The most preferred direction vector is along the [0*n*0] direction, i.e., along the *Y* axis, and accounts for about one-third of all observed loops. It must be mentioned that most of the loops labeled as

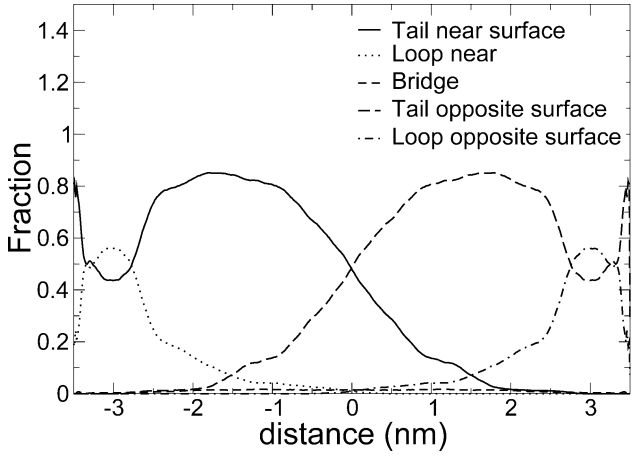

Figure 12. Fraction of total beads belonging to different chain species as a function of position relative to the center plane of the simulation box.

belonging to [0*n*0] are actually formed between crystal stems belonging to the same unit cell, i.e., the direction vector is usually [0$^1/_4$0], which furthermore implies a slight preference for the formation of topologically connected bilayers of crystal stems. The number of adjacent reentry loop conformations is estimated from the population of loops that connects proximal crystal sites on the crystal surface. For *i*PP, contributions to the adjacent reentry folds arise from the three smallest loops (of size 8, 11, and 14). The population of adjacent reentry vectors is seen to be much higher (≈45%) for *i*PP than PE (≈25%).

It is important to note that even though the thickness of interphase (defined by eq 9) is only 0.75 nm, the topological connectivity of the chains in the noncrystalline region to the crystal boundaries extends well into the amorphous region. Figure 12 illustrates this effect by showing the fraction of all beads at a given distance from the crystal surface that belong to each of the following chain populations: tails originating at the crystal surface at $Z = 0$, loops originating at the crystal surface at $Z = 0$, bridges, tails originating at the crystal surface at $Z = L$, and loops originating at the crystal surface at $Z = L$. At the center plane of the interlamellar region, ∼3.25 nm away from each lamella (the distance from the crystal surface at this point is about 5 times larger than the thickness of the interphase), ∼1% of the beads belong to loop segments originating at one of the two lamellar surfaces, compared to 1.5% that belong to bridges or tie molecules that span the interlamellar phase, and about 48.25% that belong to tails tethered at one of the two lamellar surfaces (for this molecular weight of *i*PP). This has enormous implications for the mechanical properties of the system because it suggests that entanglements between loops originating at opposing crystal surfaces could be almost as populous as bridges. Like bridges, such entangled loops would also serve to tie the two lamellae together topologically.

For a more complete understanding of local conformations, we scrutinize the distributions of states adopted by single dihedrals and pairs of adjacent dihedrals. From Figure 13 it is evident that the probability of *tg* states is the highest, approaching 80%, and is consistent with the earlier results of Suter and Flory[41] and Antoniadis et al.[42] for amorphous *i*PP melts. Both *trans* and *gauche* states appear with almost the same frequency, but it is interesting to note that the *tg* state occurs with a probability that is far higher than the product of the two constituent probabilities ($P_{tg} > P_tP_g$) due to the energetic penalties associated with both *tt* and *gg* dyads.

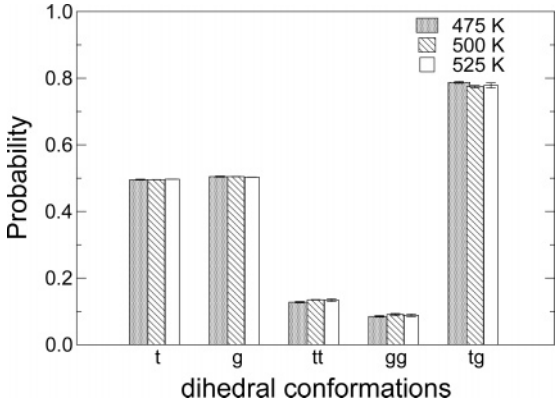

Figure 13. Distribution of torsional conformations at 475, 500, and 525 K.

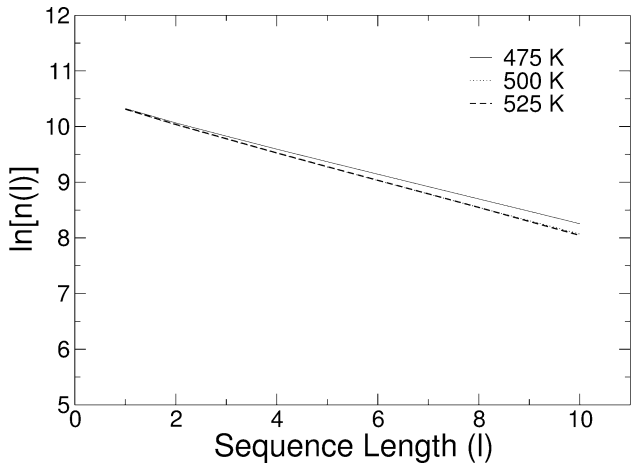

Figure 14. Distribution of alternating *t* and *g* dihedral sequences for chain segments of various sequence lengths at 475, 500, and 525 K. Sequence length *l* is defined as the number of consecutive *trans*−*gauche* or *gauche*−*trans* dyadic pairs formed by considering successive backbone dihedrals (for *tg*, $l = 1$, for *tgt*, $l = 2$, for *tgtg*, $l = 3$, etc.).

Local conformations of the chains are probed by examining the sequences of torsional angles for successive dihedrals along the backbone of polymer molecules. Figure 14 shows the number of sequences of alternating *trans* and *gauche* dihedrals for segments in the noncrystalline region. The abscissa indicates the length l (up to $l = 10$) of the sequence, calculated by enumerating consecutive *tg* or *gt* dyads in blocks of successive backbone dihedrals, i.e., for *tg* or *gt*, $l = 1$; for *tgt* or *gtg*, $l = 2$; for *tgtg* or *gtgt*, $l = 3$, etc. The sequences correspond to a distribution that follows Markovian statistics of first order.

Figure 15 shows the interfacial internal energy for the GDS computed according to the scheme outlined in ref 29; we have calculated the interfacial internal energy for *i*PP to lie in the range 0.06−0.10 J/m^2 for 475 K < T < 525 K. Experimentally, a wide range of values for the free energy of the fold surface of *i*PP have been reported, depending on the methodology employed. Burns and Turnbull[43] used optical microscopy measurements of crystal nucleation and growth to determine the free energy, with values between 0.06 and 0.095 J/m^2. Dobreva and co-workers[44] employed a nonisothermal method in which the rate dependence of crystallization temperature was used to calculate a free energy value for the fold surface of 0.12 J/m^2. Most recently, Bond and co-workers[18] studied the melting temperatures of crystallites of different thicknesses to obtain free energy values varying from 0.0252 to 0.0476 J/m^2, depending on sample synthesis (Ziegler−Natta or metallocene catalyzed) and preparation. By comparing our results with the

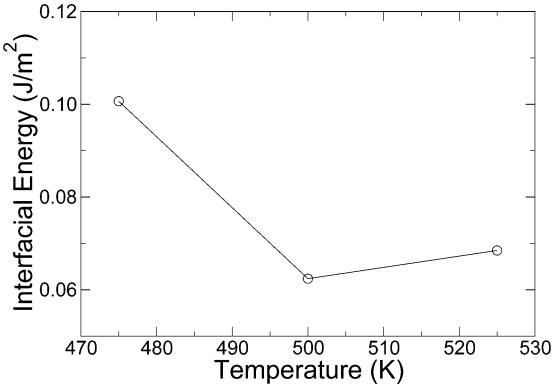

Figure 15. Interface internal energy calculated at 475, 500, and 525 K using the Gibbs dividing surface.

investigations of Bond et al.,[18] we estimate the entropic contribution to the fold surface free energy to lie between 0.02 and 0.06 J/m^2. With such a close matching of values, we have further confidence that these simulations provide a faithful and realistic representation of the interphase and amorphous interlamellar region for isotactic polypropylene.

Finally, a comparison of interlamellar properties between isotactic polypropylene and linear polyethylene can now be made. Architecturally, the distinction between the two polymers is the presence of the methyl side group on *i*PP, which necessitated the use of the expanded ensemble algorithm to promote sampling of phase space. It is also responsible for the change of crystal symmetry and crystal stem conformation. The most striking difference between the interphases of these two polymers is revealed in their density and bond order parameter profiles. As seen in earlier studies, the width of the transition region in PE is temperature-dependent and, at a comparable ΔT above the melting point, is ∼0.96 nm[29] (Figure 6). Furthermore, from Figure 3 of ref 25, we see that the decay of P_2 for PE occurs over ∼2 nm. It is clear from a comparison of PE and *i*PP that the interphase thickness is greater in PE than *i*PP by a factor of ∼2. This is likely due to the stiffer backbone of the linear PE chain (characteristic ratio, $C_\infty = 7.3$) relative to *i*PP ($C_\infty = 5.9$).

The differences in backbone dihedral sequences are also manifested in the topology of short loops, which reveal a higher probability for adjacent reentry loops in *i*PP compared to PE. In particular, the influence of distance between crystal stems, chain backbone stiffness, and temperature on loop reentry vectors that were postulated in ref 25 are reinforced by these simulations of *i*PP. The higher flexibility of the *i*PP chain reduces the energy penalty involved in connecting adjacent crystal stems with short chain sequences, resulting in more adjacent reentry loops. Both polymers exhibit a weak temperature dependence, showing a higher preference for shorter loop segments with increasing temperature.

4. Conclusions

We report the first study of the crystal−amorphous interphase in a polymer with side groups, using Monte Carlo molecular simulations with a united atom force-field model to mimic isotactic polypropylene. Use of the expanded ensemble technique in which replica exchanges are performed in Hamiltonian space between systems with different side group interaction energies was necessary to realize efficient sampling and adequate equilibration that permit the system to explore different chain connectivities with respect to the crystal surface. These topology changing moves allow the crystal−amorphous system

to recreate the metastable equilibrium that exists long after crystallization and molecular ordering has been completed. The population distributions follow an exponential decay with chain length. Heuristics for the connectivity of the interlamellar phase that were deduced from the prototypical linear chain of PE are also found to hold for *i*PP. The influence of the distance between crystal stems, backbone stiffness, and weak temperature dependence is reflected by the topological populations. In addition, heuristics based on interphase density and chain flexibility can be deduced from the current work. It is found that isotactic polypropylene, being a more flexible polymer than polyethylene according to lower C_∞, is disposed toward a larger fraction of adjacent reentry loop conformations ($\approx$45%) than PE. Mass density and bond orientation order profiles also reveal that the dissipation of density and order from the crystal surface into the amorphous melt occurs over a relatively short distance for *i*PP. This is quantitatively mirrored by the thickness of the transition region between crystal and melt calculated by invoking the concept of the Gibbs dividing surface. Furthermore, because of density effects, a steeper decay in tail and loop populations with number of beads is observed for those tails and loops located predominantly within the interphase. Our simulations reveal that the interphase thickness is smaller for *i*PP than for PE.

A juxtaposition of results for *i*PP and PE shows that the contrasting responses of the two polymers can be traced back to the differences in their molecular architecture. The effect of the more flexible *i*PP backbone is apparent not only in the smaller thickness of the interphase but also in the prevalence of adjacent reentry loops.

Acknowledgment. The authors thank Dr. Markus Hütter for valuable comments on this research and on the manuscript. Financial assistance was provided by the Center for Advanced Engineering Fibers and Films through the ERC program of the National Science Foundation under Award ECC-9731680.

References and Notes

(1) Flory, P. J. *J. Chem. Phys.* **1949**, *17*, 223.
(2) Natta, G.; Corradini, P. *Rubber Chem. Technol.* **1952**, *33*, 703.
(3) Natta, G.; Corradini, P. *J. Polym. Sci.* **1959**, *39*, 29.
(4) Flory, P. J. *J. Am. Chem. Soc.* **1962**, *84*, 2857.
(5) Keller, A. *MTP Int. Rev. Sci.* **1972**, *8*, 105.
(6) Fischer, E. W. *Z. Naturforsch. A* **1957**, *12*, 753.
(7) Till, P. H. *J. Polym. Sci.* **1957**, *24*, 301.
(8) Storks, K. H. *J. Am. Chem. Soc.* **1958**, *60*, 1753.
(9) Flory, P. J.; Yoon, D. Y.; Dill, K. A. *Macromolecules* **1984**, *17*, 862.
(10) Strobl, G. *The Physics of Polymers*; Springer: Berlin, 1997.
(11) Russell, T. P.; Ito, H.; Wignall, G. D. *Macromolecules* **1988**, *21*, 1703.
(12) Akpalu, Y. A.; Ames, E. J. *J. Chem. Phys.* **1999**, *111*, 8686.
(13) Akpalu, Y. A.; Kielhorn, L.; Hsiao, B. S.; Stein, R. S.; Russell, T. P.; van Egmond, J.; Muthukumar, M. *Macromolecules* **1999**, *32*, 765.
(14) Mandelkern, L. *Acc. Chem. Res.* **1990**, *23*, 380.
(15) Mandelkern, L. In *Crystallization of Polymers*; Dosiere, M., Ed.; Kluwer Academic Publishers: Dordrecht, 1993.
(16) Saito, S.; Moteki, Y.; Nakagawa, M.; Horii, F.; Kitamaru, R. *Macromolecules* **1990**, *23*, 3256.
(17) Nielsen, A. S.; Batchelder, D. N.; Pyrz, R. *Polymer* **2002**, *43*, 2671.
(18) Bond, E. B.; Spruill, J. E.; Lin, J. S. *J. Polym. Sci., Part B: Polym. Phys.* **1999**, *37*, 3050.
(19) Pütz, M.; Curro, J. G.; Grest, G. S. *J. Chem. Phys.* **2001**, *114*, 2847.
(20) Martin, M. G.; Siepmann, J. I. *J. Phys. Chem. B* **1999**, *103*, 4508.
(21) In 't Veld, P. J.; Rutledge, G. C. *Macromolecules* **2003**, *36*, 7358.
(22) Maitland, G. C.; Rigby, M.; Smith, E. B.; Wakeham, W. A. *Intermolecular Forces*; Clarendon: Oxford, 1981.
(23) Krishna Pant, P. V.; Theodorou, D. N. *Macromolecules* **1995**, *28*, 7224.
(24) Mavrantzas, V. G.; Boone, T. D.; Zervopoulou, E.; Theodorou, D. N. *Macromolecules* **1999**, *32*, 5072.
(25) In 't Veld, P. J.; Hütter, M.; Rutledge, G. C. *Macromolecules* **2006**, *39*, 439.
(26) Balijepalli, S.; Rutledge, G. C. *J. Chem. Phys.* **1998**, *109*, 6523.
(27) Karaiskos, E.; deJoannis, J.; Anastasiadis, S. H.; Bitsanis, I. A. *Macromol. Theory Simul.* **2004**, *13*, 762.
(28) Frenkel, D.; Smit, B. *Understanding Molecular Simulations: From Algorithms to Applications*; Academic Press: New York, 2002.
(29) Hütter, M.; In 't Veld, P. J.; Rutledge, G. C. *Polymer* **2006**, *47*, 5494.
(30) Kofke, D. A. *J. Chem. Phys.* **2002**, *117*, 6911.
(31) Khare, A. A.; Rutledge, G. C. *J. Chem. Phys.* **1999**, *110*, 3063.
(32) Khare, A. A.; Rutledge, G. C. *J. Phys. Chem.* **2000**, *104*, 3639.
(33) Natta, G.; Corradini, P. *Nuovo Cimento, Suppl.* **1960**, *15*, 9.
(34) Lotz, B.; Wittman, J. C.; Lovinger, A. J. *Polymer* **1996**, *37*, 4979.
(35) Khoury, F. *J. Res. Natl. Bur. Stand.* **1966**, *70A*, 29.
(36) Maier, R.-D.; Thomann, R.; Kressler, J.; Mülhaupt, R.; Rudolf, B. *J. Polym. Sci., Part B: Polym. Phys.* **1997**, *35*, 1135.
(37) Rutledge, G. C. *J. Macromol. Sci., Part B: Phys.* **2002**, *B41*, 909.
(38) Spyriouni, T.; Economou, I. G.; Theodorou, D. N. *Macromolecules* **1997**, *30*, 4744.
(39) de Pablo, J. J.; Laso, M.; Suter, U. W. *J. Chem. Phys.* **1992**, *96*, 6157.
(40) Gautam, S.; Balijepalli, S.; Rutledge, G. C. *Macromolecules* **2000**, *33*, 9136.
(41) Suter, U. W.; Flory, P. J. *Macromolecules* **1975**, *8*, 765.
(42) Antoniadis, S. J.; Samara, C. T.; Theodorou, D. N. *Macromolecules* **1999**, *32*, 8635.
(43) Burns, J. R.; Turnbull, D. *J. Appl. Phys.* **1966**, *37*, 4021.
(44) Dobreva, A.; Alonso, M.; Gonzalez, M.; Gonzalez, A.; de Saja, J. A. *Thermochim. Acta* **1995**, *258*, 197.

MA0703958